Design, analysis and testing of thermoplastic welded stiffened panels to investigate skin-stringer separation in post-buckling

van Dooren, Kevin; Bisagni, Chiara

DOI
10.1016/j.compositesb.2023.111033

Publication date
2023

Document Version
Final published version

Published in
Composites Part B: Engineering

Citation (APA)
van Dooren, K., & Bisagni, C. (2023). Design, analysis and testing of thermoplastic welded stiffened panels to investigate skin-stringer separation in post-buckling. *Composites Part B: Engineering*, *267*, Article 111033. https://doi.org/10.1016/j.compositesb.2023.111033

Composites Part B 267 (2023) 111033

Contents lists available at ScienceDirect

Composites Part B

journal homepage: www.elsevier.com/locate/composites

Design, analysis and testing of thermoplastic welded stiffened panels to investigate skin-stringer separation in post-buckling

Kevin van Dooren, Chiara Bisagni *

Delft University of Technology, Faculty of Aerospace Engineering, Delft, The Netherlands

ARTICLE INFO

Keywords:
Buckling
Thermoplastic composite
Welding
Testing
Virtual Crack Closure Technique
Failure characterisation

ABSTRACT

Thermoplastic composite three-stringer panels with omega stiffeners and conduction welded joints are designed, analysed and tested until final failure to investigate the performance of the welded joint in post-buckling. The three-stringer panels are designed to be structurally representative of the fuselage demonstrator of the Clean Sky 2 project STUNNING. A simplified model of the fuselage keel section is analysed by finite element analysis, using the virtual crack closure technique to model skin-stringer separation of the welded joint. The post-buckling and skin-stringer separation behaviour of the fuselage section is then adopted as the reference for the design of the three-stringer panels. Two panels are then tested. The test setup utilises digital image correlation to measure the deformation of the panels, and a high-speed camera to capture the final failure mode. The panels failed in post-buckling due to the separation of the middle stringer, with unstable separation growth followed by separation of the outer stringers and then stringer fracture. The numerical analysis of the panels, with geometrical imperfections included, is able to predict the structural behaviour accurately, with only minor differences in buckling shape and separation behaviour.

1. Introduction

The aeronautical field has shown an increase in research and development of thermoplastic composite materials. The use of thermoplastic composites can aid in the sustainability of aeronautical structures, and in decreasing the manufacturing costs [1,2]. It offers possibilities for a wide range of manufacturing techniques, such as thermoplastic welding [3] and co-consolidation processes [4,5]. Other advantages are high toughness, recycle possibilities, long shelf life and chemical resistance [6].

Aeronautical composite structures usually consist of a skin with stiffening elements, and can present buckling under compression and shear loads. Weight savings could be achieved by allowing the structures to buckle below the ultimate load, which necessitates an increased understanding of the post-buckling and failure behaviour, but the failure of composite structures is difficult to predict due to the complexity and catastrophic nature [7].

In the post-buckling field of stiffened structures, the skin shows large out-of-plane displacement which causes high stresses at the interface between the skin and stringer. These high stresses can cause skin-stringer separation [8]. The majority of research on skin-stringer separation has been conducted on thermoset composites [9–11], and only limited research is available regarding thermoplastic composites [12]. Thermoplastics show higher fracture toughness compared to the more brittle thermoset materials, as demonstrated by Reeder [13], which can highly influence the skin-stringer separation behaviour.

The focus of the research field on thermoplastic composite stiffened structures has been primarily on manufacturing and testing, with limited research on predicting buckling and post-buckling behaviour. Flanagan et al. [14] compared joining techniques, namely induction welding and adhesive bonding, using press-formed stringers. Peeters et al. [15] designed and manufactured a thermoplastic section omega-shaped stringer. Oliveri et al. [16] designed, manufactured and tested a wingbox, which utilised laser-assisted automated tape placement process with winding and in-situ consolidation.

Tijs et al. [3,6] evaluated conduction welded joints in single lap shear specimens and characterised inter-laminar behaviour considering fibre bridging and R-curve effects, both experimentally and numerically. Brito et al. [17,18] investigated ultrasonic welded single lap shear specimens, and the effect of misaligned adherents and how to improve process efficiency and weld quality.

Skin-stringer separation has been researched on stiffened structures with both blade stringers and omega stringers, mainly made of thermoset composites [19,20]. Single stringer specimens with a blade stringer were investigated by Orifici et al. [21] in both pristine and damaged states with a debond. The panels failed in compression due

* Corresponding author.
E-mail address: c.bisagni@tudelft.nl (C. Bisagni).

https://doi.org/10.1016/j.compositesb.2023.111033
Received 8 July 2023; Received in revised form 1 September 2023; Accepted 2 October 2023
Available online 7 October 2023

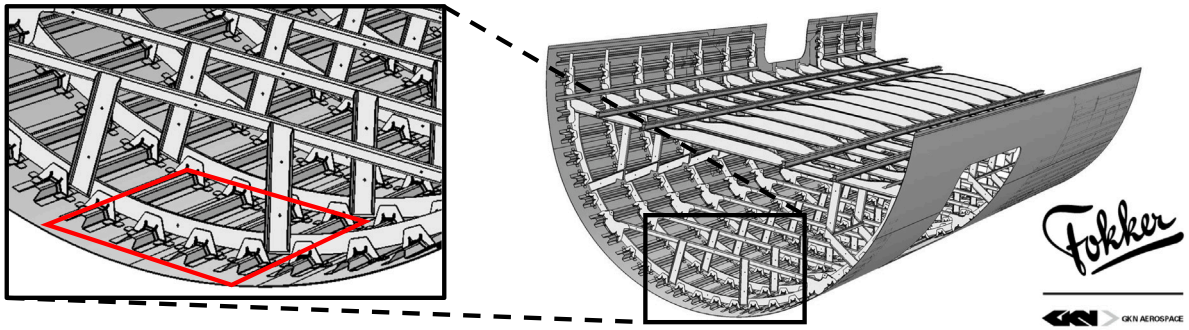

Fig. 1. Lower half of the STUNNING Multifunctional Fuselage Demonstrator, with the keel section highlighted [1,2].

to skin-stringer separation in post-buckling, with the pristine panels collapsing immediately at the start of separation, and the pre-damaged panel collapsing after debond growth. The experimental data of Orifici et al. [21] was used for validation by Riccio et al. [22], who presented a numerical procedure for skin-stringer separation using both Virtual Crack Closure Technique (VCCT) and Cohesive Zone Method (CZM). Multi-stringer panels with blade stringers were designed and analysed by Degenhardt et al. [23], and the experimental data was used for validation of a numerical prediction by Orifici et al. [24]. The post-buckling behaviour was difficult to correlate with the experimental data, due to the geometrical imperfections highly influencing the post-buckling shape.

Bisagni et al. [25] designed Single-Stringer Compression Specimens (SSCS) by analysis for the investigation of skin-stringer separation of stiffened structures with omega stringers. The numerical methodology included CZM for skin-stringer separation and a continuum damage model for crippling of the omega stiffeners. Specimens with and without artificial damage were tested, and the numerical prediction achieved good correlation. Vescovini et al. [9] analysed the failure behaviour of the SSCS with a simplified model and introduced a global/local damage approach. The fatigue behaviour of SSCS was analysed numerically by Raimondo et al. [26] with a VCCT-based approach for skin-stringer separation. Single-stringer specimens with an initial delamination were tested in fatigue by Paz et al. [27], investigating the effect of different load levels and load ratios. A skin-stringer separation study by Kootte [28] used single-stringer specimens, but instead of in-plane loading, out-of-plane displacement was applied directly to the skin to approximate the post-buckling shape.

This research is part of the STUNNING project, which designed and manufactured the lower half of a thermoplastic multi-functional fuselage demonstrator [1,2]. The fuselage makes use of manufacturing techniques such as press-forming, compression moulding and thermoplastic welding of several critical joints. In this paper, a three-stringer panel is designed with the goal of approximating the structural behaviour of the fuselage keel section, as it is considered the critical section due to its low skin thickness and susceptibility to impact damage, for instance, by tool drops. The design of the panel is conducted with the objective of showing similar structural and failure behaviour and taking into account manufacturing and testing constraints. A numerical and experimental methodology is developed to evaluate the strength of the conduction welded joint between skin and stringer in post-buckling. Two panels, of which the skin is manufactured by NLR — Netherlands Aerospace Centre, and the conduction welding of the stringers to the skin is performed by GKN Fokker, are tested until collapse and analysed with Abaqus.

2. Thermoplastic fuselage section

The lower half of the fuselage of the STUNNING project is shown in Fig. 1. The keel section is considered as the area of interest, due to its low skin thickness, and is highlighted in red. A fuselage section approximating the keel section is modelled and shown in Fig. 2. The fuselage section is modelled up to the cargo beams and includes the vertical beams, frames and clips. The geometries and joining methods used for the beams, frames, brackets and clips are simplified to lower the complexity of the models, and because these parts are not of interest in this research. The total length of the section is 2005 mm, the total width is 2664 mm, the outer radius is 1926 mm, the stringer pitch is 212 mm, and the frame spacing is 635 mm. The omega stringer geometry is reported in Fig. 3.

Table 1
T700/LM-PAEK Toray CETEX TC1225 material properties [29].

E_{11} [MPa]	E_{22} [MPa]	ν_{12} [–]	G_{12} [MPa]	F^t_1 [MPa]	F^c_1 [MPa]	F^t_2 [MPa]	F^c_2 [MPa]	F_{12} [MPa]
116 800	9100	0.36	4100	2442	1250	94	212	99

Table 2
Layups of fuselage section.

	Layup	Thickness (mm)
Skin 12	[−45/45/0/90/−45/45] s	2.208
Skin 16	[−45/45/0/90/0/90/−45/45] s	2.944
Stringer	[45/0/−45/0/$\underline{90}$] s	1.656

The skin and stringers are made of Toray CETEX TC1225 T700/LM-PAEK 194 gsm with a nominal ply thickness of 0.184 mm. Properties of a similar material, Toray CETEX TC1225 T700/LM-PAEK 145 gsm, are used for the analysis with a ply thickness of 0.184 mm, and are reported in Table 1 [29]. The skin layups of the fuselage section are also simplified to only two different layups, a 12 ply layup in the middle nine bays, and a 16 ply layup for the two outer bays on each side of the section. The stringers have a 9 ply layup. The layups are reported in Table 2.

3. Numerical analysis of fuselage section

The numerical analyses are performed using the commercial software Abaqus 2021 [30]. The fuselage section is analysed with dynamic implicit analysis, with non-linear geometry activated. The total time-step is 1 s with an initial and maximum time-step of 0.01 s, and a minimum time-step of 1e−08 s.

The fuselage is loaded in bending using a linear displacement field that applies compression to the fuselage section, with the bottom of the section in maximum compression, as illustrated in Fig. 4. Boundary conditions applied to the free edges of the fuselage section, which are the edges of the skin and frame ends, constrain the circumferential degree of freedom, as illustrated in Fig. 5, and leave the radial degree of freedom unconstrained.

The area of interest of the fuselage section is in between the two middle frames and includes the middle three bays, as shown in Fig. 2. The area of interest has a mesh size of 2.5 mm, while the adjacent

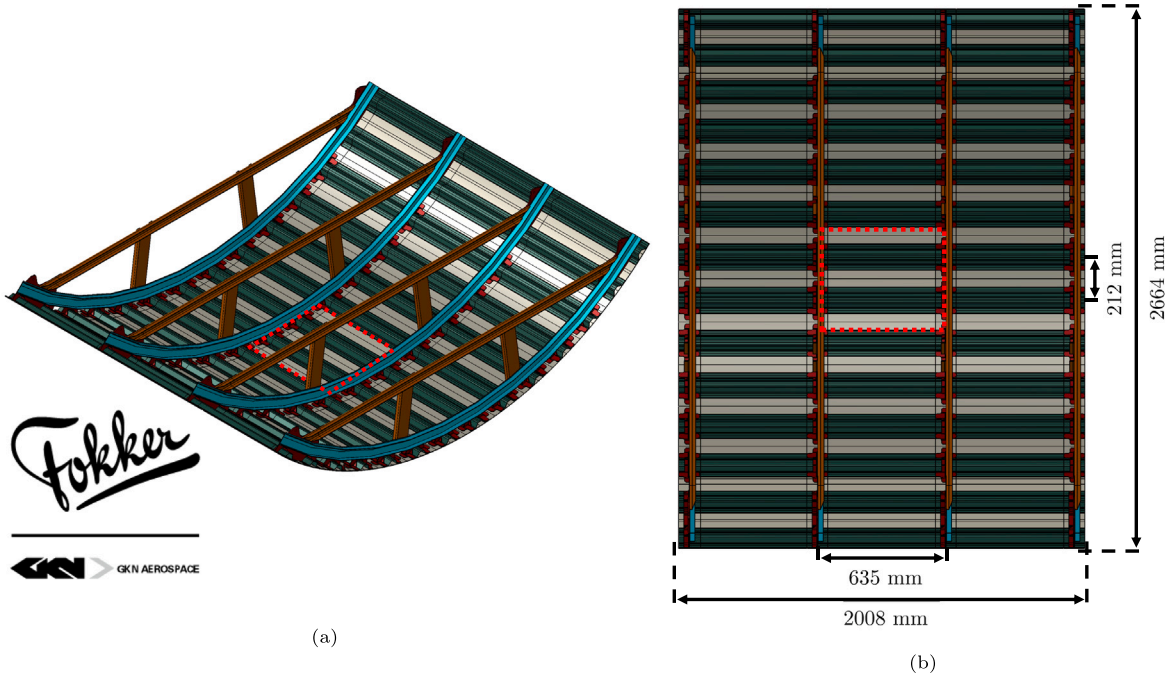

Fig. 2. Fuselage section with highlighted area of interest: (a): iso-view; (b): top-view.

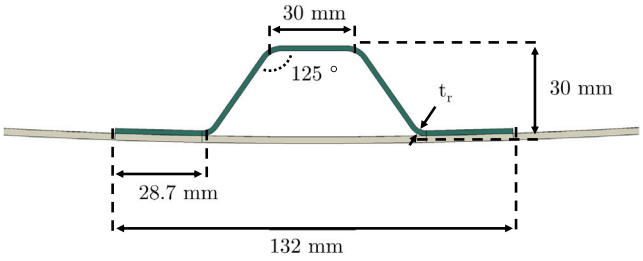

Fig. 3. Omega stringer geometry.

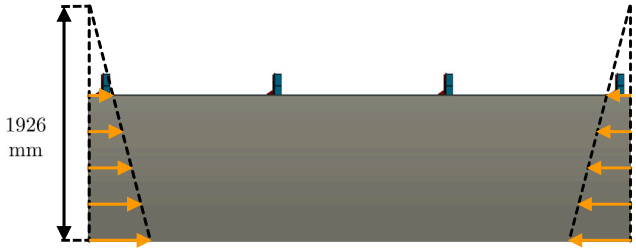

Fig. 4. Side-view of fuselage section model showing bending load-case.

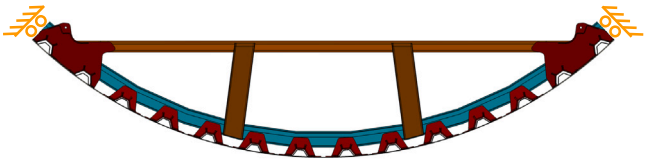

Fig. 5. Cross-section of fuselage section showing circumferential constraint.

areas are meshed coarser when feasible with a mesh size of 5 mm to improve computational efficiency. The clips and brackets have a mesh size of 5 mm, and the vertical strut and cargo beam have a mesh size of 10 mm. The laminated parts utilise SC8R continuum shell elements, and the brackets and clips of the fuselage section utilise the C3D10 tetrahedral element.

Table 3
Fracture properties of skin-stringer interface [33].

G_{IC} [kJ/m^2]	G_{IIC} [kJ/m^2]	G_{IIIC} [kJ/m^2]	η [–]
0.969	1.719	1.719	2.284

The joints between the separate geometries are modelled with three different techniques, namely shared nodes, rigid body ties and the Virtual Crack Closure Technique (VCCT) [31,32]. Parts with mismatching meshes, such as the frame, vertical strut, clips, brackets and cargo beam, are modelled with rigid body ties. VCCT is applied for the welded joint of the two middle stringers in the area of interest, while the welded joints of the adjacent areas adopt shared nodes.

It is assumed that there is only crack growth in the skin-stringer interface, with no crack migration into other interfaces, to lower the complexity of the model. This assumption is based on the unwelded regions on both sides of the weld, which makes it more likely to separate the welded interface instead of the interlaminar interfaces. The VCCT definition utilises the Benzeggagh–Kenane (BK) criterion for mode-mixity, in which the critical equivalent strain energy release rate G_{equivC} and the equivalent strain energy release rate G_{equiv} are calculated with Eqs. (1) and (2), respectively. The critical equivalent strain energy release rate is calculated using the fracture toughness G_{IC}, G_{IIC} and G_{IIIC} of the interface and the BK parameter η. G_{IC}, G_{IIC} and η are based on a similar material AS4/PEEK [33], which utilises a matrix material from the same thermoplastic polymer family of polyaryletherketones, and the properties are reported in Table 3. It is assumed that G_{IIC} and G_{IIIC} are equal. The strain energy release rate is calculated for the three different modes, G_I, G_{II} and G_{III}, at each node and the sum is the equivalent strain energy release rate. The fracture criterion is reported in Eq. (3). It allows a node to be released at the crack tip when G_{equiv} divided by G_{equivC} is higher than 1.

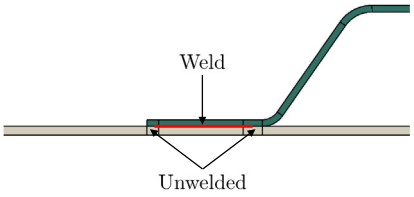

Fig. 6. Weld between skin and stringer.

$$G_{equivC} = G_{IC} + (G_{IIC} - G_{IC}) \left(\frac{G_{II} + G_{III}}{G_I + G_{II} + G_{III}} \right)^{\eta} \quad (1)$$

$$G_{equiv} = G_I + G_{II} + G_{III} \quad (2)$$

$$f = \frac{G_{equiv}}{G_{equivC}} \geq 1.0 \quad (3)$$

A default fracture tolerance of 0.2 is used for the VCCT definition, with an unstable crack growth tolerance of 1. The unstable crack growth tolerance can improve convergence and lower computational time. It allows the analysis to release multiple nodes ahead of the crack-tip and allows the analysis to use larger time steps during unstable crack growth. While the default unstable crack growth tolerance in Abaqus is infinity, in this study it is chosen to limit this tolerance to have a larger number of data-points during unstable crack growth events. A contact stabilisation factor of 1e−4 is used to stabilise contact, and node-to-surface contact discretisation is implemented with the stringer side as master surface and skin side as slave surface.

One of the main benefits of VCCT is that it allows for a coarser mesh to model skin-stringer separation, in comparison to other methods. The downside is that a pre-crack is required to utilise VCCT, which

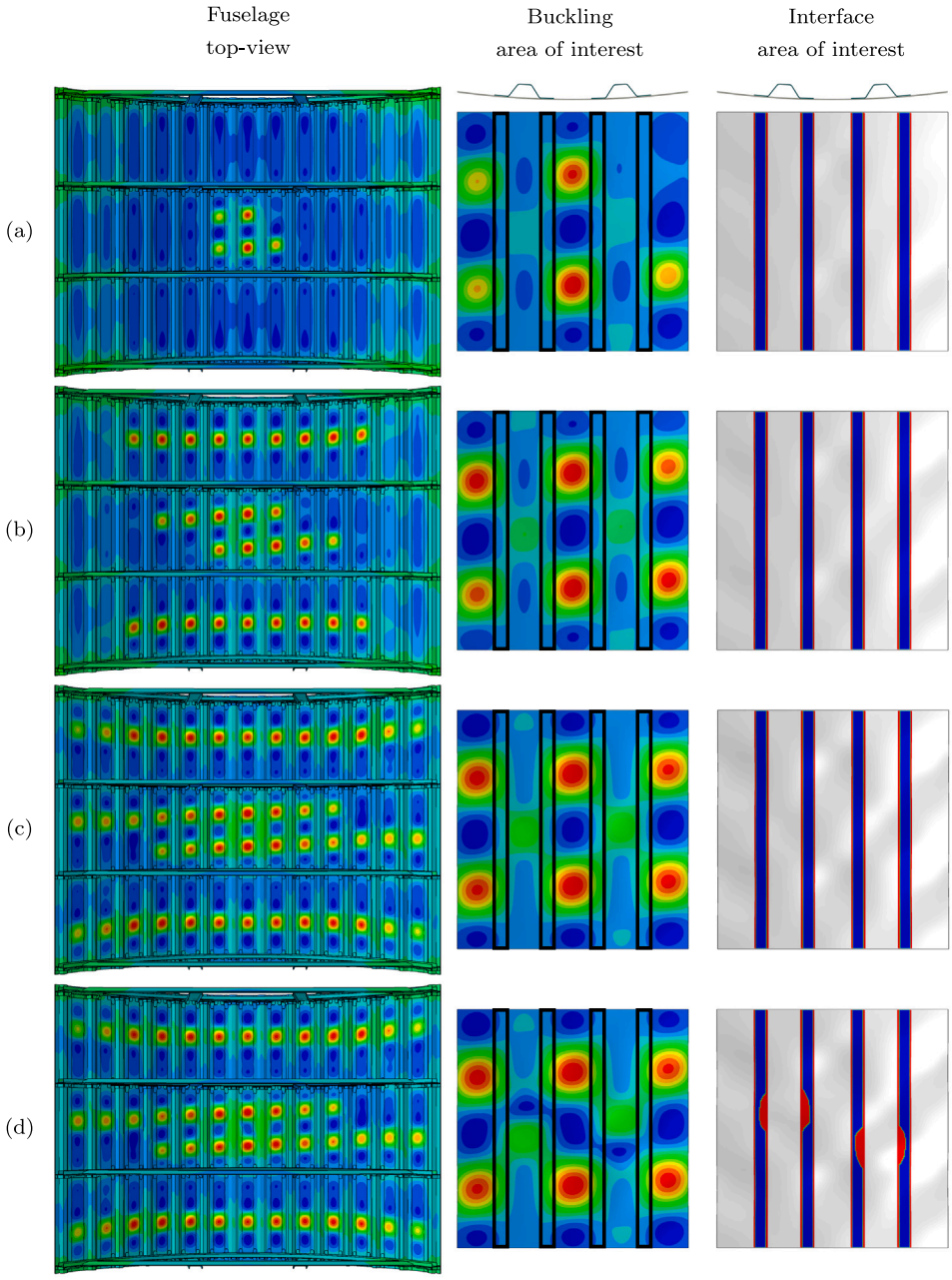

Fig. 7. Radial displacement of fuselage section, radial displacement and interface state of area of interest, at different levels of bending with a longitudinal displacement of: (a) 5.36 mm; (b) 6.27 mm; (c) 8.23 mm; (d) 8.24 mm.

generally limits the use of this method to structures with initial damage. This downside can however be overcome in this study due to the geometry of the conduction welded joint. There are small unwelded areas adjacent to the joint, as shown in Fig. 6, which are considered as a pre-crack. The weld is initially assumed to be 21 mm wide, based on visual inspection of an early manufacturing sample. This weld width of 21 mm is used for the fuselage section analysis and the preliminary panel analysis.

The analysis includes first-ply failure criteria, to investigate if material failure happens before skin-stringer separation. The criteria of Hashin, Tsai–Wu and Tsai–Hill are included. The strength properties are reported in Table 1 [29]. The buckling shape of the fuselage section is investigated. Contour plots of the out-of-plane displacement are shown at different levels of longitudinal bending, and consequentially different maximum longitudinal displacement, in Fig. 7. The contour plots show the out-of-plane radial displacement of the fuselage section and a close-up of the area of interest, and the interface state of the two stringers in the area of interest. The area of interest consists of the middle three bays and two stringers in between the two middle frames and has the highest level of compression. This area also limits itself to the two stringers and adjacent bays where skin-stringer separation is modelled with VCCT. In the contour plots of the area of interest, the interface state of the welded flange is blue for the intact interface and red for the pre-crack and separation. The stringers are hidden, and an outline of the stringer flanges is shown in black, to allow seeing the radial displacement in the bay and underneath the stringer.

At a maximum applied longitudinal displacement of 5.36 mm, the skin in the middle of the section in between the two middle frames starts to buckle with a five half-wave buckling shape (Fig. 7(a)). The half-waves in the bay have a much higher radial displacement compared to the half-waves underneath the stringer, with the half-waves at the top and bottom barely visible. The half-wave length underneath the stringer and in the bay is similar, but the sign of the radial displacement is inversed for the adjacent waves in the circumferential direction. The buckling shape continuously evolves, with the remaining bays in between the middle frames displaying an initial three half-wave buckling shapes followed by a five half-wave buckling shape(Fig. 7(b)). At a maximum longitudinal displacement of 8.23 mm (Fig. 7(c)) all bays have buckled, with the top and middle bays showing mostly three half-wave buckling shapes, with some of the bays starting to form a fifth half-wave.

At a maximum displacement of 8.24 mm (Fig. 7(d)), failure due to skin-stringer separation starts, with separation developing from underneath the stringer. It is seen that the outward half-waves in the radial direction in the bay and underneath the stringer start to connect, which is called tunnelling. Separation starts almost simultaneously in two stringers, with similar elliptical crack front shapes. Once separation starts, it is unstable, and the stringer totally separates in one separation event.

4. Panel design and manufacturing

The structural behaviour of the STUNNING fuselage keel section is the reference behaviour for the design of the three-stringer panels, with the buckling and failure behaviour as the main focus. The design also needs to take manufacturing and testing constraints into account. The three stringers allow for bay buckling on both sides of the middle stringer, such that the structural behaviour of the middle stringer can be representative of the fuselage section.

The panels have the same stringer pitch and nominal stringer geometry as the STUNNING fuselage lower half, shown in Figs. 2 and 3, respectively. The nominal width and length of the panels are equal to 556 mm and 500 mm, respectively. The panel length corresponds to the maximum possible welding length available at the time of the design. The geometry of the three-stringer panel is shown in Fig. 8. The panels are made of the same CF/LM-PAEK material as used in the

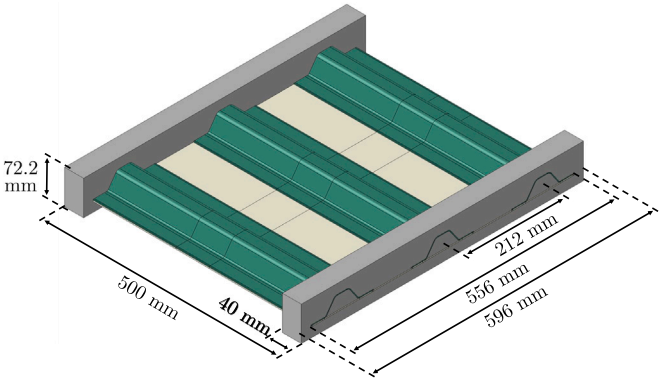

Fig. 8. Three-stringer panel.

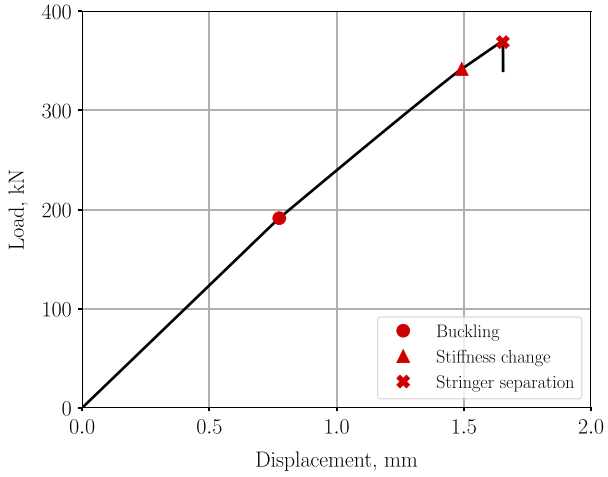

Fig. 9. Load–displacement curve of the panel preliminary analysis.

Table 4
Layups of three-stringer panel.

	Layup	Thickness (mm)
Skin	[−45/45/90/0/90/0] s	2.208
Stringer	[45/0/−45/0/90] s	1.656

STUNNING fuselage, of which the material properties are reported in Table 1 [29]. The skin layup is different compared to the keel section of the STUNNING fuselage to achieve a more conservative stress field in post-buckling, while the stringer layup is the same as in the STUNNING fuselage. The layups are reported in Table 4.

The structural behaviour of the three-stringer test panel without imperfections is analysed and compared to the reference behaviour of the fuselage section. The preliminary analysis of the panel is conducted without any imperfections and considering a 21 mm weld width. A displacement boundary condition is used for the panel to apply the load case of pure compression. A reference point is positioned on each loading face of the model, with a rigid body tie to the loading face. One reference point is clamped, while the other reference point is constrained in all degrees of freedom except for the longitudinal displacement. A longitudinal displacement of 2.5 mm is applied, resulting in a displacement rate of 2.5 mm/s.

The laminated parts of the panel use a mesh size of 2.5 mm, and a mesh size varying between 2.5 mm and 10 mm is used for the potting material to improve computational efficiency. The laminated parts consist of SC8R continuum shell elements, and the C3D8R solid element is applied for the potting material. VCCT is utilised for the test

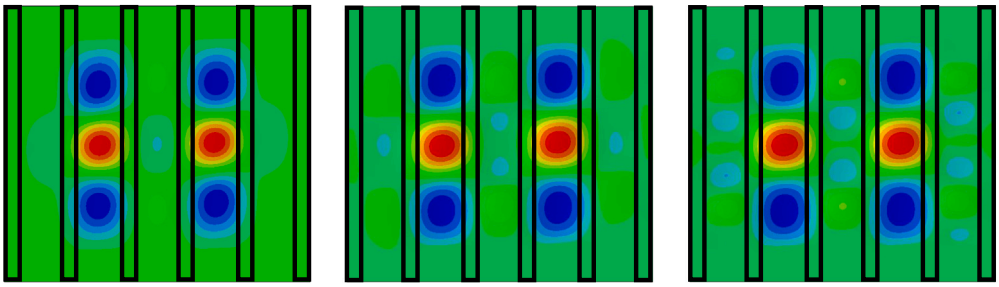

Fig. 10. Buckling shapes of the panel preliminary analysis: (a) 0.78 mm/191 kN; (b) 1.48 mm/338 kN ; (c) 1.65 mm/370 kN.

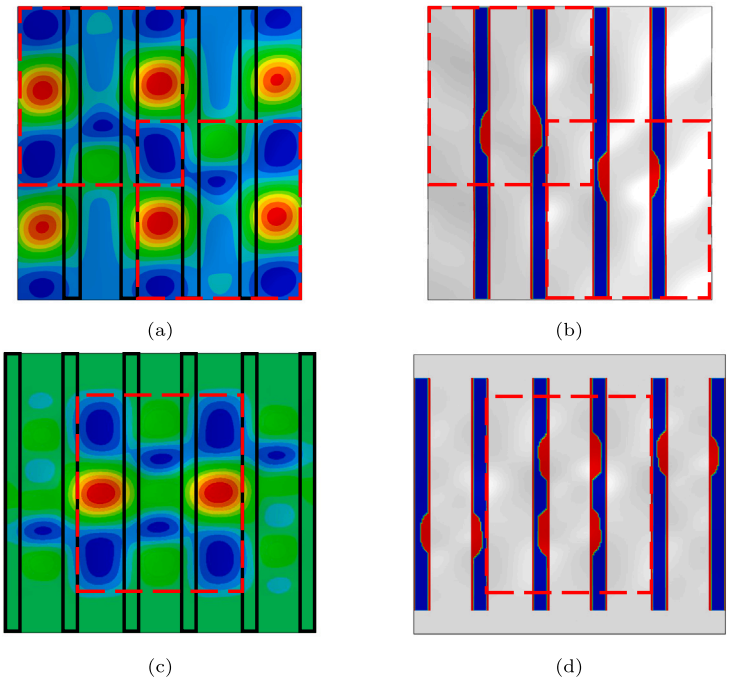

Fig. 11. Comparison of skin-stringer separation behaviour from the analyses: (a) buckling shape of fuselage section; (b) welded skin-stringer interface state of fuselage section; (c) buckling shape of the panel; (d) welded skin-stringer interface state of the panel.

panel in all welded joints in between the potting, while the geometries inside the potting material adopt shared nodes.

The load–displacement graph of the three-stringer panel is shown in Fig. 9. The linear stiffness before buckling is 248.2 kN/mm. Local buckling occurs at an approximate load of 192 kN and displacement of 0.78 mm. At 338 kN the panel presents a small buckling shape change. Panel failure occurs at a load of 370 kN and displacement of 1.65 mm due to skin-stringer separation.

The panel displays a three half-wave buckling shape, as reported in Fig. 10(a), with one half-wave in an inwards direction and two half-waves in an outwards direction. The average half-wave length of the panel and the fuselage section is very similar. At a load of 338 kN, the buckling shape changes underneath the stringer, as shown in Fig. 10(b).

Two main aspects of the skin-stringer separation behaviour of the fuselage section and of the three-stringer panel are compared. The first aspect is the out-of-plane deformation when skin-stringer separation occurs, shown in Fig. 11(a) and (c) for the fuselage and the panel, respectively. The second aspect is the shape and location of the crack front, shown in Fig. 11(b) and (d) for the fuselage section and the panel, respectively. To compare the structural behaviour of the fuselage section and the panel, an area with a similar size and similar buckling shape is selected on each structure and highlighted with red dashed squares. During separation, both structures show a similar tunnelling behaviour underneath the stringer between inwards half-waves, within the highlighted area. The panel displays two tunnels per highlighted area, while the fuselage section displays one tunnel per highlighted area. The weld interface shows the same difference in the number of failure locations, that can be caused by the difference in boundary conditions. In any case, both the fuselage section and the panel show similar separation behaviour, starting from underneath the stringer and presenting an elliptical crack front.

Two nominally identical three-stringer panels are then manufactured. Project partner NLR — Netherlands Aerospace Centre manufactured the skin by automatic tape laying followed by autoclave consolidation. Project partner GKN Fokker uses conduction welding to join the stringers to the skin. Conduction welding makes use of a heating element, that is pressed on the stringer flange to apply pressure and heat, and weld the stringer flange to the skin. A panel as received is shown in Fig. 12(a). The panels are then prepared for the tests. The first step consists of casting epoxy potting onto both ends of the panels for load introduction, and then the loading faces are trimmed in a milling machine to minimise loading imperfections. This is followed by attaching strain gauges and wiring. A panel with potting and strain gauges is shown in Fig. 12(b).

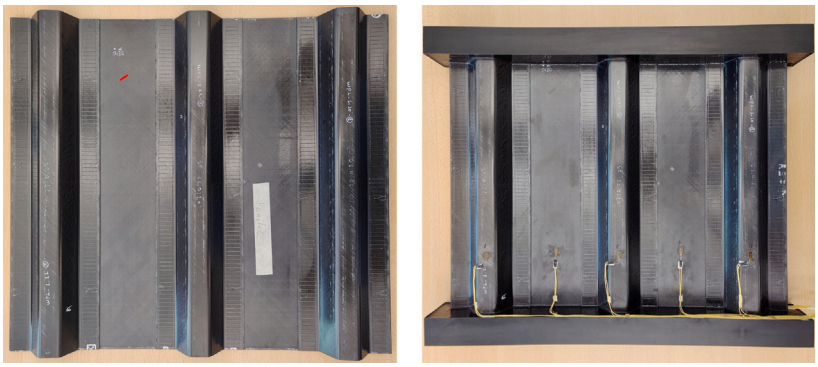

(a) (b)

Fig. 12. Test panels: (a) as received; (b) with potting and strain gauges.

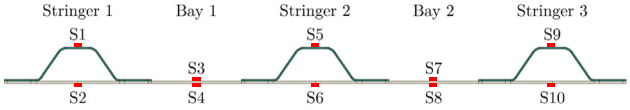

Fig. 13. Strain gauge locations.

A total of 10 strain gauges are attached, 135 mm from the bottom loading face, and the locations are reported in Fig. 13. A strain gauge is attached on top of each stringer cap and the bottom of the skin underneath each stringer. Then, strain gauges are attached back to back to the skin in the middle of each bay. The strain measurements are used to determine load imperfections, load distribution and load redistribution due to buckling and failure. The last step of the preparation for the tests consists of applying white paint with black speckles for DIC measurements.

5. Test setup

The two three-stringer panels with welded interface are tested at Delft University of Technology using an MTS test machine. The tests are executed to investigate the buckling, post-buckling and skin-stringer separation behaviour of the three-stringer panels, and to validate the numerical analysis. The test panels are placed in between the compression plate and the base, and a pre-load of 2 kN is applied. The loading rate is 0.1 mm/min until final failure, after which the loading stops automatically. The test setup is shown from the stringer-side of the panel in Fig. 14(a) and a top-view illustration of the test setup is shown in Fig. 14(b).

Three Laser Distance Sensors (LDS) are used to measure the longitudinal displacement of the compression plate in three different locations, which also allows to determine if a loading imperfection is occurring.

The displacement field is measured from both the stringer and skin side by two DIC systems. Both systems use two 5 MP cameras, and post-processing is done using VIC3D 8. This measurement allows to determine the post-buckling shape of the panels from the out-of-plane displacement, and the longitudinal shortening from the in-plane displacement of the potting.

The strain measurements, the load from the test machine, the displacement measurement by LDS and the pictures for DIC are recorded every 3 s, leading to approximately 500 data points per test.

Three additional cameras are used to capture the test. A GoPro is placed on one of the sides of the panel to capture the stringer-side of the panel for a close-up of any buckling shape changes or crack growth events. Two cameras are placed further away, one on the stringer-side and one on the skin-side of the panel, to capture the whole panel and test setup. A high-speed camera is used to capture the final failure from the stringer-side of the panels, at 10 000 fps.

6. Panel measurements

The global shape of the three-stringer panels is measured from the skin-side before the start of the test campaign using DIC.

The geometrical imperfections of panels 1 and 2 are shown in Fig. 15. The panels show a similar curved imperfection in the transverse direction, with the edges of the panel curved inwards. The total magnitude of the imperfections is 11.76 mm. The imperfection has a slight skew, rotated anti-clockwise. The orientation of the skew is likely caused by the outer −45 ply of the layup. When inspecting the imperfection of the panels more closely, it can be seen that the largest curvature is in the welding region. The curvature of the panels is most likely caused by the local heating during welding, leading to thermal stresses. The thickness of the skin and stringers are measured with a micrometer. The skin is found to be thinner compared to the nominal, with an average thickness of 2.14 mm. The flat sections of the stringers have an average thickness of 1.66 mm which is approximately the nominal thickness. It is however seen that in the middle of the radius from stringer flange to web, the thickness is lower, shown as t_r in Fig. 3, with an approximate minimum thickness of 1.15–1.20 mm.

The stringer spacing and panel length are also measured. The stringer spacing of panel 2 matches the nominal design of 212 mm. The middle stringer of panel 1 has an average offset of 2 mm from the centre line of the panel and is slightly angled. The panel length is approximately 489 mm for both panels.

The numerical models for panels 1 and 2 are updated to take into account the measurements. In particular, numerical models of the two panels have geometrical imperfections included as measured by DIC. The method to include the measured imperfections is based on including a node file of the imperfection in the analysis [12]. This node file is created by a linear analysis, where the out-of-plane imperfection is applied as a displacement field to the skin. The final shape, which now replicates the out-of-plane imperfection, is outputted as a node file which can be included in further analysis. This node file only transfers the deformation and not the stress field.

The models also include imperfections of laminate thickness and stringer alignment imperfection. The models do not include residual stresses from the manufacturing process, to prevent additional complexity of the models and analysis.

After inspection of the failed test panels, it is found that the weld had a varying weld width which is less wide, with a lower bound of 18 mm in the middle region of the panel. The updated numerical models of panels 1 and 2 are therefore considered with a weld width of 18 mm.

7. Experimental and numerical results

The test results of the three-stringer panels are reported in this section and are compared to the results from the numerical analysis performed using the updated analysis.

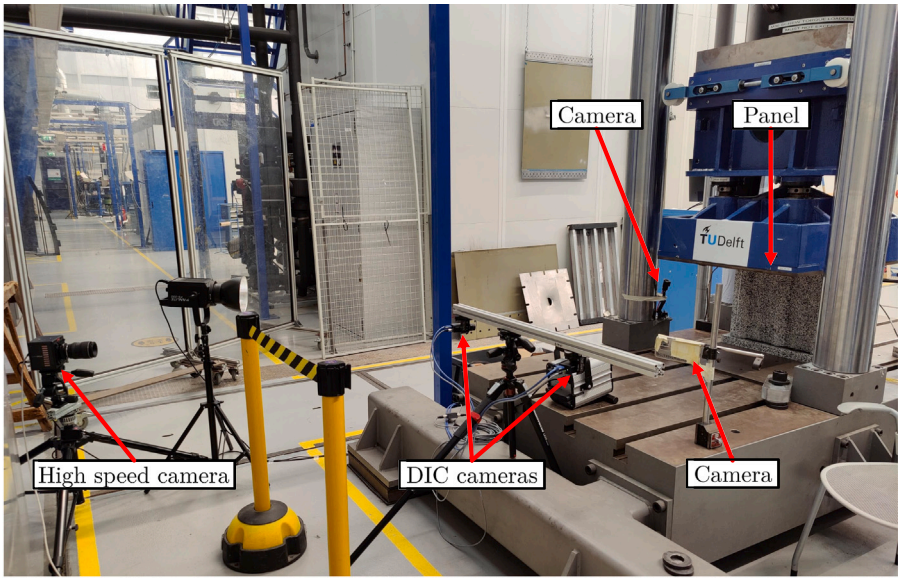

(a)

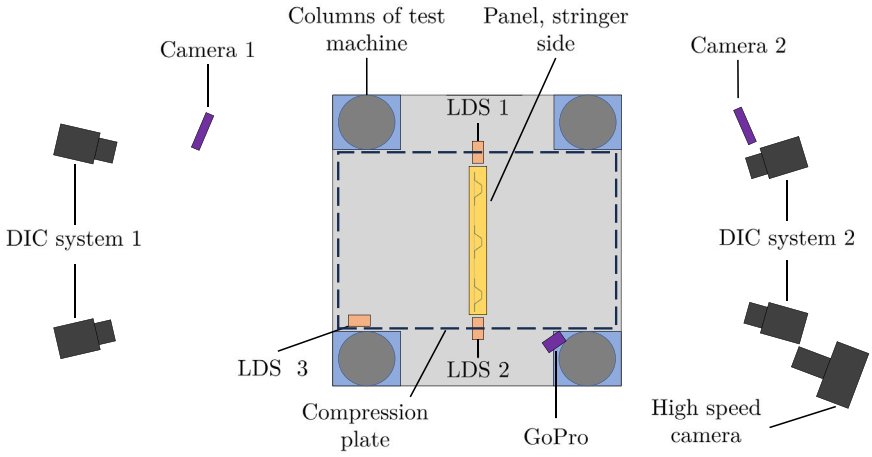

(b)

Fig. 14. Test setup: (a) test setup photo stringer side; (b) test setup schematic top-view.

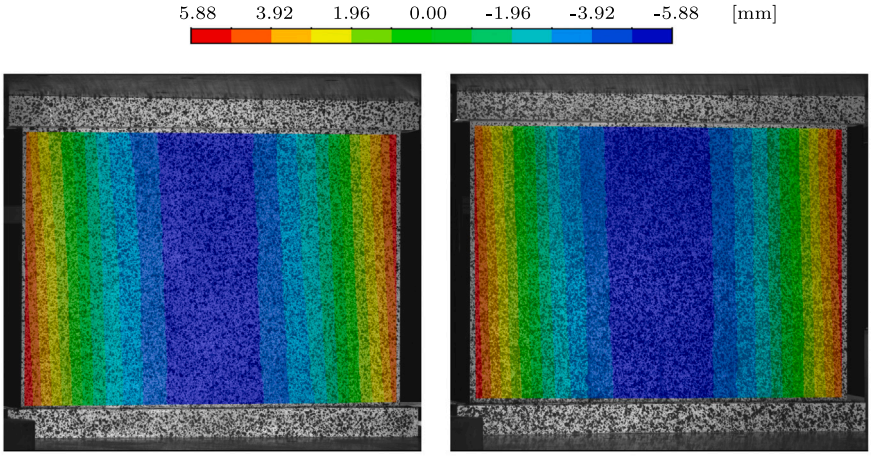

(a) (b)

Fig. 15. Out-of-plane imperfections: (a) panel 1; (b) panel 2.

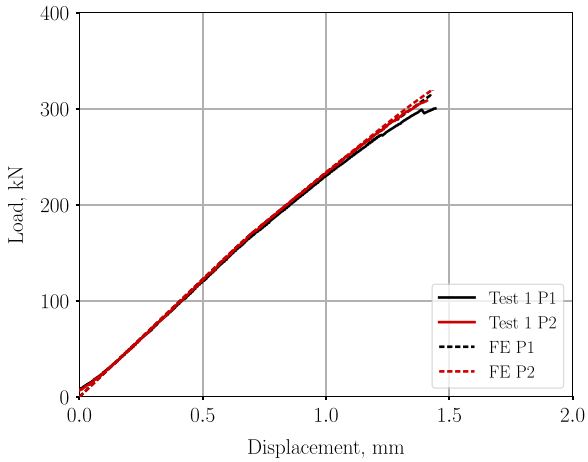

Fig. 16. Load–displacement curves from tests and numerical analysis.

7.1. Load versus displacement curves

The load measured by the load cell of the testing machine is reported in Fig. 16, as a function of the average displacement measured by the two LDS. The panels show settling behaviour till approximately 30 kN after which they present a linear stiffness of approximately 240.2 kN/mm and 244.1 kN/mm for panels 1 and 2, respectively, until buckling. Panel 1 starts to locally buckle at an approximate load of 155 kN and panel 2 at a load of 165 kN. In the post-buckling field, panel 1 shows a higher reduction of stiffness compared to panel 2. This is caused by a buckling shape change, which starts gradually at 245 kN and shows a small load drop at 275 kN due to a sudden shape change. Panel 2 does not show any load drops before failure. The panels fail due to skin-stringer separation at a load of 301 kN and 309 kN for panels 1 and 2, respectively, as reported in Table 5.

The numerical analyses conducted using dynamic implicit analysis show a stiffness of 244.6 kN/mm and 244.9 kN/mm for panels 1 and 2, respectively. This is a 1.8% and 0.3% difference in comparison with the test results. The numerical analysis of both panels shows buckling at approximately 160 kN, which is a difference of 3.2% and 3.0% for panels 1 and 2, respectively. In comparison to the test results the initial post-buckling stiffness is similar, but at higher loads, the stiffness is over-predicted. The higher over-prediction for panel 1 is caused by smaller load drops due to buckling shape changes that occur at 245 kN and 285 kN. The numerical analysis predicts panel collapse due to skin-stringer separation at a load of 314 kN and 320 kN for panels 1 and 2 respectively, as reported in Table 5. This is an over-prediction of 4.3% for panel 1 and 3.6% for panel 2 in comparison to the test results. The difference between the experimental and numerical results can be caused by not taking into account the loading imperfections, the difference in material properties and the slight skew of the middle stringer of panel 1 in the numerical models.

Table 5
Pre-buckling stiffness, buckling load and maximum load from tests and numerical analysis.

	Pre-buckling stiffness			Buckling load			Maximum load		
	Test [kN/mm]	FE [kN/mm]	Diff. [%]	Test [kN]	FE [kN]	Diff. [%]	Test [kN]	FE [kN]	Diff. [%]
Panel 1	240.2	244.6	1.8	155	160	3.2	301	314	4.3
Panel 2	244.1	244.9	0.3	165	160	3.0	309	320	3.6

7.2. Load versus strain curves

The strains measured on the caps of panels 1 and 2 are shown in Fig. 17(a) and (b), respectively. On panel 1 they show diverging behaviour initially, most likely due to loading imperfections, and a similar gradient until the buckling shape changes and the skin and stringer separate. The strains in the caps of panel 2 diverge less in comparison to panel 1, with stringers 1 and 2 showing similar strains in pre-buckling and stringer 3 showing lower strains. In post-buckling, it is seen that the strains in stringers 2 and 3 show similar gradients, while the strains in stringer 1 show a higher gradient.

The numerical analysis predicts the strains in the stringers reasonably well, with the main difference being the initial loading.

The strains measured at the bottom of the skin underneath the stringers of panels 1 and 2 are shown in Fig. 18(a) and (b), respectively. The strains of panel 1 show only minor differences in pre-buckling, with slightly lower strains underneath stringer 3. In post-buckling, the strains start to diverge, with sudden drops and increases of strain due to buckling shape changes and a separation event. The strains in the stringers of panel 2 show a slightly larger difference in pre-buckling, with higher strains underneath stringer 1. In post-buckling, the strains underneath stringers 1 and 2 converge, with lower strains underneath stringer 3. No sudden changes in strains are seen in comparison to panel 1.

The numerical analysis predicts the pre-buckling strains well. For panel 1 the predicted strains diverge less in post-buckling in comparison to the test result, and the jumps in strain happen at different load levels. For panel 2 the post-buckling strains are predicted more accurately, with the strains being under-predicted close to the failure load.

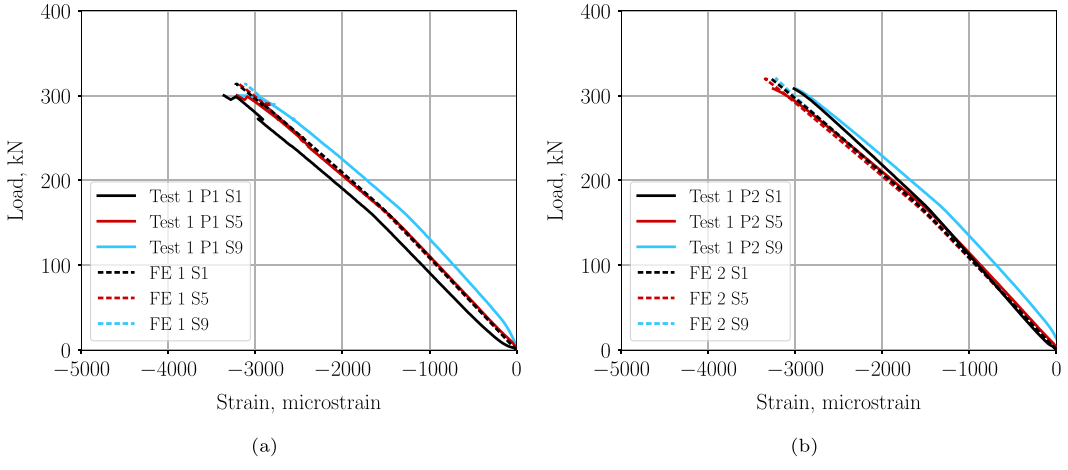

Fig. 17. Experimental and numerical compressive strains in stringer caps: (a) panel 1; (b) panel 2.

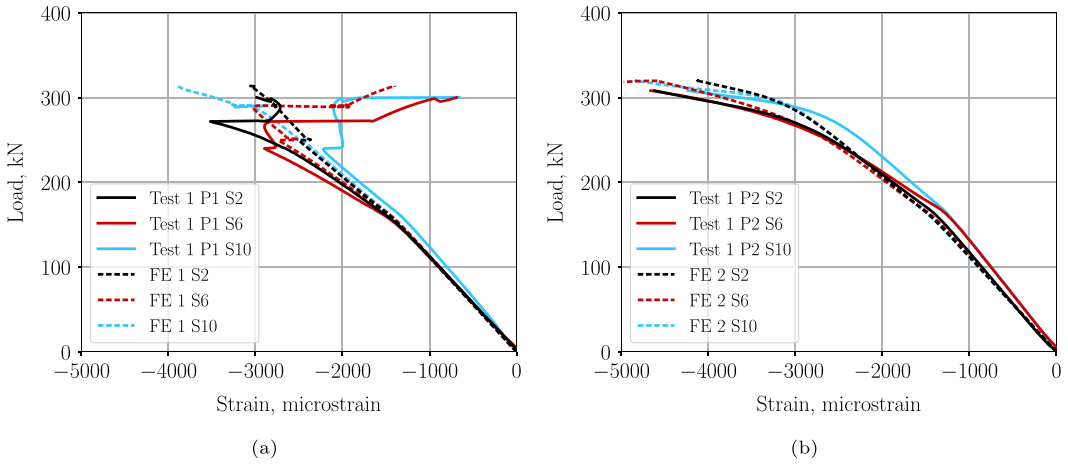

Fig. 18. Experimental and numerical compressive strains in the skin below stringer: (a) panel 1; (b) panel 2.

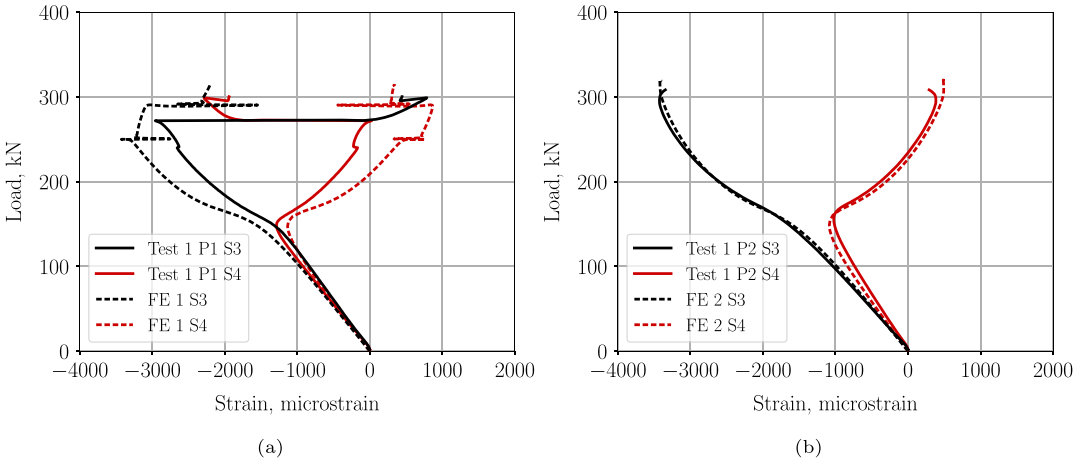

Fig. 19. Experimental and numerical compressive strains in the skin of bay 1: (a) panel 1; (b) panel 2.

The strains measured back-to-back in bay 1 of panels 1 and 2 are shown in Fig. 19(a) and (b), respectively. The strains in pre-buckling of panel 1 show a small difference, which indicates a small bending component. In post-buckling, the strains diverge due to high levels of bending, with a small jump when the buckling shape of bay 2 changes and a large jump when bay 1 shows a buckling shape change. The strains in bay 1 of panel 2 present a higher bending component, both before buckling and in the post-buckling field, with no sudden jumps. Close to the failure load, it is also seen that the strain gradient changes sign.

The numerical analysis results of panel 1 show close agreement in pre-buckling strain gradient compared to the test, but with an opposite bending component. In post-buckling, the strains diverge more in comparison to the test results, which corresponds to a higher bending component, and the jumps in strain are less severe and at different load levels. These differences can be accounted to differences in buckling shape between the test and numerical analysis. The numerical analysis results of panel 2 show a closer agreement with the test, both in pre-buckling and post-buckling.

The strains measured back-to-back in bay 2 of panels 1 and 2 are shown in Fig. 20(a) and (b), respectively. The strains in bay 2 of panel 1 show similar behaviour as bay 1, with sudden changes in strains in the post-buckling field due to the buckling shape changes. The strains in bay 2 of panel 1 are similar to bay 1, with a large bending component and no sudden changes.

The numerical analysis predicts the strains in bay 2 of panel 1 well in pre-buckling and in the post-buckling field until buckling shape changes start to occur. For bay 2 of panel 2, the strains are predicted well, with an under-prediction of the bending component in both pre-buckling and post-buckling.

7.3. Evolution of buckling shape

The out-of-plane displacement from the DIC measurement and the numerical analysis of panels 1 and 2 are reported in Figs. 21 and 22, respectively, highlighting the buckling shape and the evolution of the shape in the post-buckling field. Positive displacement corresponds to inwards direction, and negative displacement corresponds to outwards direction.

Panel 1 shows an initial three half-wave buckling shape, with a slight skew in the vertical half-wave position. At 245 kN a buckling shape change occurs in bay 2 with a fourth half-wave at the bottom of the bay, and at 273 kN another buckling shape change happens with a fourth half-wave at the bottom of bay 1. After the buckling shape changes in the bay, the number of half-waves underneath the stringer also increases. At the maximum load, the displacement is higher on the right side of the panel, which is due to a skin-stringer separation event that occurred at 300 kN.

Panel 2 shows a three half-wave buckling shape with no buckling shape change in the bays, and at higher loads the number of half-waves increases underneath the stringer. The three half-wave buckling shape does not show a skew in vertical position of the half-waves as panel 1, which might be due to differences in imperfections. The maximum inwards out-of-plane displacement is similar between panels 1 and 2,

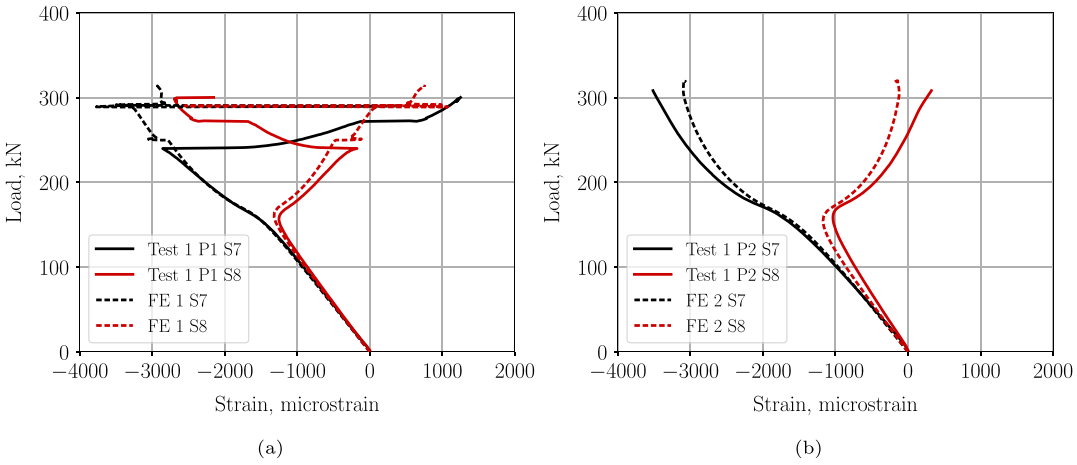

Fig. 20. Experimental and numerical compressive strains in the skin of bay 2: (a) panel 1; (b) panel 2.

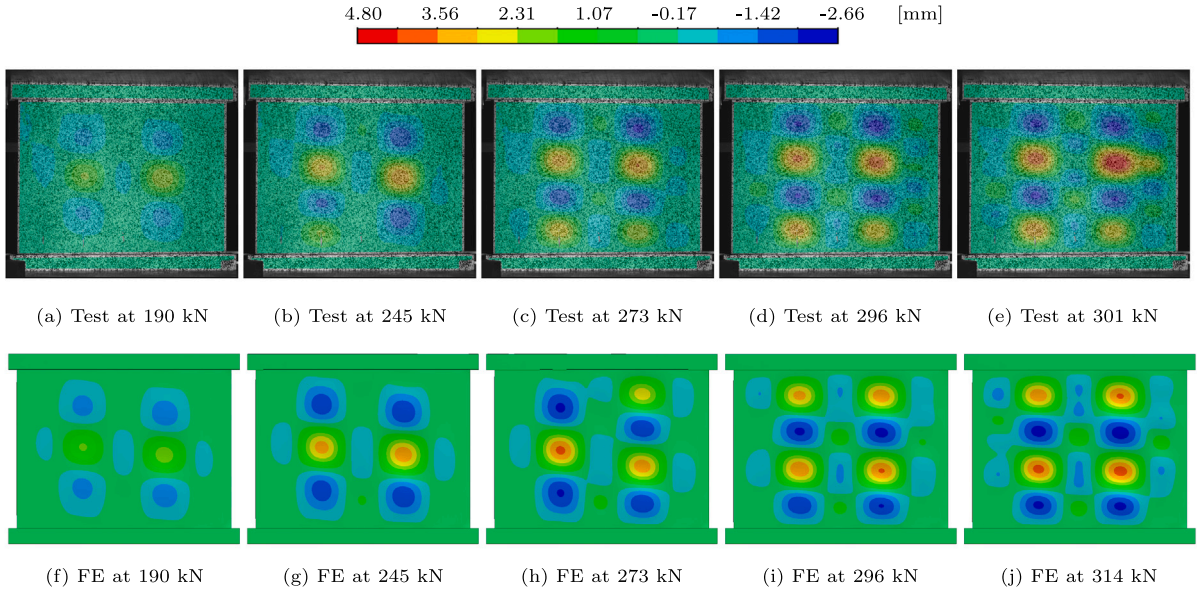

Fig. 21. Experimental and numerical out-of-plane displacement of panel 1.

but the maximum outwards displacement of panel 2 is higher. The difference in final buckling shape might lead to the small difference in failure load and it can indicate that the four half-wave buckling shape is slightly more critical. Both panels showed an increase in the number of half-waves underneath the stringer, and these half-waves become more prominent in terms of out-of-plane displacement close to the failure load.

The numerical analysis predicts the initial three half-wave buckling shape of both panels 1 and 2. The numerical analysis of panel 1 also shows buckling shape changes in the bay to four half-waves, but the changes occur at higher loads and the fourth half-waves form at the top of the panel. This difference can be caused due to the fact that the stringer alignment imperfections are not taken into account. The numerical analysis of panel 2 is able to predict the post-buckling behaviour well, with the evolution of the half-waves underneath the stringer and no shape changes in the bay. The maximum inwards displacement of panel 1 is lower in the numerical analysis, while the maximum outwards displacement shows good agreement. The maximum inwards and outwards displacement of panel 2 is predicted well, with the outwards displacement being slightly over-predicted.

7.4. Final failure

The final failure of panels 1 and 2 is captured by the high-speed camera at 10 000 fps.

Panel 1 shows a skin-stringer separation event in stringer 1 which did not lead to final failure. The location of this separation event is indicated by the blue arrow in Fig. 23(a). It occurs at a load of 299 kN and causes a load drop to 295 kN. It is visible from the deformation of the flange and web of the stringer, which causes a change in the shadow on the web. The event could also be heard and seen on the normal camera footage and causes a sudden increase in the out-of-plane displacement measured by the DIC. From the camera footage, it appears that the separation starts from underneath the stringer and stops approximately halfway through the stringer flange. The test is then continued until a load of 301 kN where the panel fails due to skin-stringer separation. Final failure starts by separation of the middle stringer, with the first separation location shown by the red arrow in Fig. 23(a). This separation appears to start from underneath the stringer and grows both in longitudinal direction and width direction towards the bay.

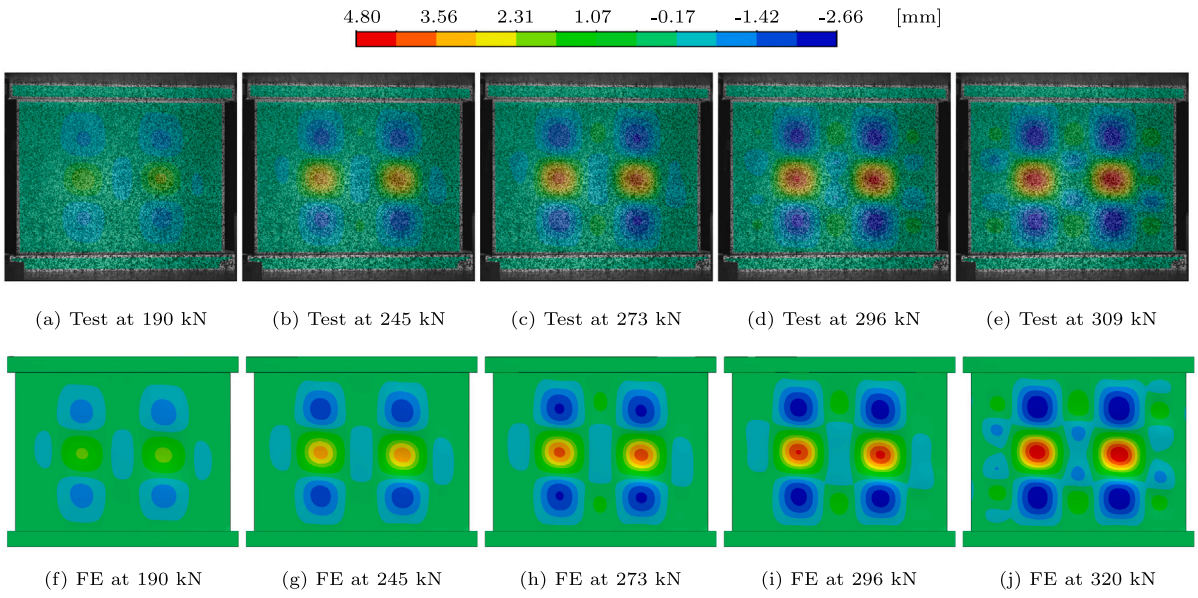

Fig. 22. Experimental and numerical out-of-plane displacement of panel 2.

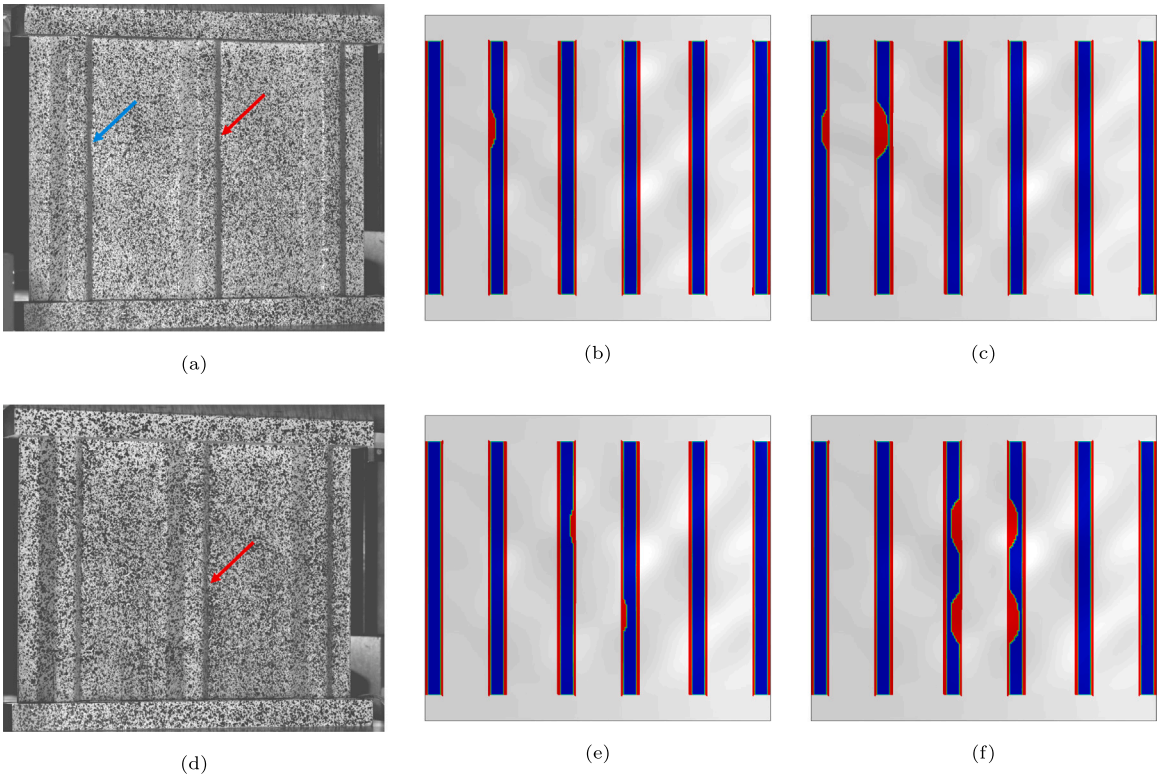

Fig. 23. Comparison of failure behaviour: (a) start of failure of panel 1 during test; (b) start of failure of panel 1 analysis; (c) propagation of panel 1 analysis; (d) start of failure of panel 2 during test; (e) start of failure of panel 2 analysis; (f) propagation of panel 2 analysis.

Panel 2 shows final failure at a load of 309 kN due to skin-stringer separation of the middle stringer, as reported in Fig. 23(d). Separation starts at a different location than panel 1, most likely caused by the different buckling shape, but grows in a similar manner from underneath the stringer.

The numerical results are shown in Fig. 23(b–c) and (e–f) for panels 1 and 2, respectively. The figures report the skin of the panels with contour plots of the interface states, where blue means intact interface and red means separation or unwelded regions next to the weld. The numerical analysis predicts that the final failure of panel 1 starts with skin-stringer separation of stringer 1 as shown in Fig. 23(b–c). The separation grows in longitudinal and width directions with an elliptical crack front. The failure location is similar to the location of the first skin-stringer separation event in the test of panel 1. The numerical analysis of panel 2 predicts that final failure starts with skin-stringer separation of the middle stringer as shown in Fig. 23(e–f). Separation starts in two locations simultaneously, shortly followed by two other locations, all in the middle stringer with elliptical crack fronts. The

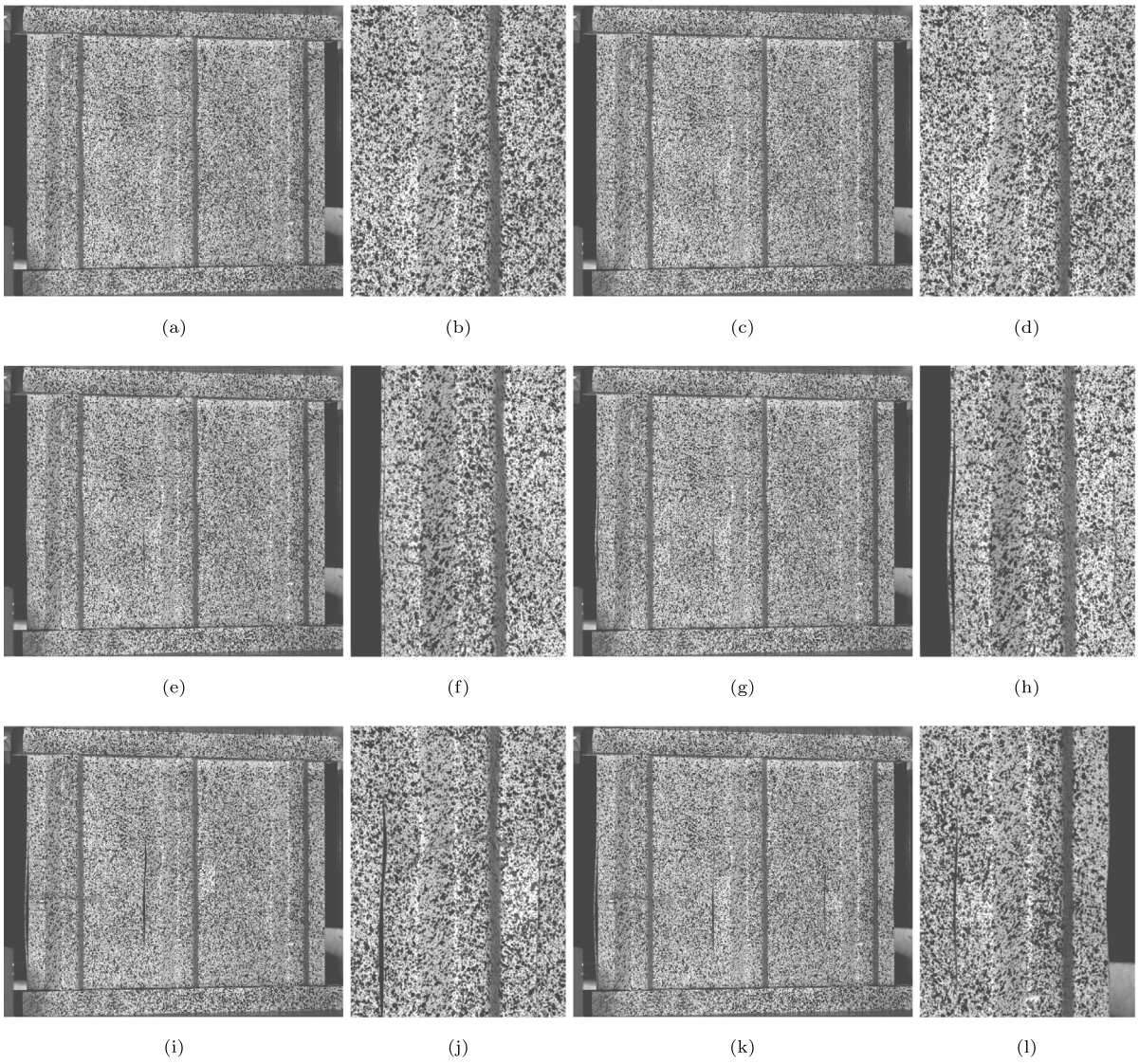

Fig. 24. Failure sequence of panel 1: (a) separation in middle stringer; (b) close-up of middle stringer; (c) propagation of separation in middle stringer; (d) close-up of middle stringer; (e) separation in left stringer; (f) close-up of left stringer; (g) fracture of left stringer; (h) close-up of left stringer; (i) fracture of middle stringer; (j) close-up of fracture of middle stringer; (k) separation in right stringer; (l) close-up of right stringer.

failure locations are slightly different compared to what is seen in the test, which can be caused by differences in buckling shape and imperfections.

The final failure sequence of panel 1 is shown in Fig. 24. It starts with skin-stringer separation in the right flange of the middle stringer, Fig. 24(a–b). The separation propagates in outward direction towards the bay, and the left flange also separates with similar behaviour, Fig. 24(c–d). Separation then starts in the left stringer, first in the right flange, followed by the left flange, Fig. 24(e–f). This is followed by the fracture of the left stringer, Fig. 24(g-h), and then of the middle stringer, Fig. 24(i–j). Lastly, the right stringer separates, Fig. 24(k–l). The failure sequences occur within approximately 3 ms.

The failure sequence of panel 2 is not reported, as it shows similar behaviour. It starts with skin-stringer separation in the middle stringer, followed by the separation of the left and right stringers, which happen simultaneously. Then, the middle stringer fractures, closely followed by the fracture of the right stringer.

From the high-speed footage of both panels, it can be concluded that skin-stringer separation is the critical failure mode leading to final failure.

7.5. Post-failure

Photos of panel 1 after failure are shown in Fig. 25(a–b). The panel shows large separated areas and large outward deformation of the skin. The left and middle stringer are fractured approximately in the middle of the panel, and several stringer flanges have delaminations. The skin appears to be mostly intact, with only minor damage close to the failed welds. These findings are supported by the c-scan results reported in Fig. 26(a), where it is possible to note that the left and middle stringers have partial separations from underneath the stringer at the top of the panel, with elliptical crack fronts, while the right stringer has almost no intact interface left.

Photos of panel 2 after failure are shown in Fig. 25(c–d). The panel has large separated areas towards the top, with large outward skin deformation. It can be noted that the large separated areas are in the opposite direction compared to panel 1, which has more separation in the downward direction. The middle and right stringer are fractured approximately in the middle of the panel, and the stringer flanges show delaminations. The skin seems to be mostly intact, judging from both

(a) (b) (c) (d)

Fig. 25. Post-failure photos: (a) panel 1 right side; (b) panel 1 left side; (c) panel 2 right side; (d) panel 2 left side.

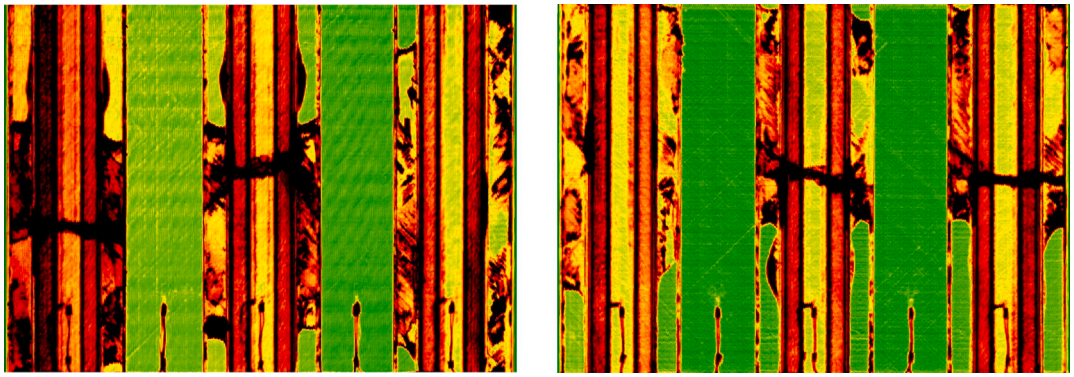

(a) (b)

Fig. 26. Post-failure c-scan: (a) panel 1; (b) panel 2.

visual inspection and the c-scan results reported in Fig. 26(b). From the c-scan, it can also be seen that the interface at the bottom of the middle stringer shows separations in both flanges with elliptical crack fronts.

7.6. Weld fracture surface

The middle stringer of panel 1 is removed after the test to investigate the weld fracture surface, which is shown in Fig. 27. The area in between the red dashes is separated during the test, while the areas outside of the red dashes are separated after the test when the stringer is removed from the panel. The weld fracture surface can be identified by the darker and rough surface in comparison to the surrounding areas. It can be seen that there is limited damage to the skin-side of the interface, with only small amounts of fibres delaminated from the skin. The stringer flanges have several areas where the top ply has delaminated. There are also fibres fractured off the stringer, which remain attached on the skin-side of the interface. On both the left and right weld Fig. 27 (a + c), light grey marks indicate an elliptical crack front during propagation. The width of the weld varies slightly along the length, ranging from approximately 17 to 19 mm. However, the weld might seem wider than it actually is, due to the possibility of the adjacent surfaces being damaged by the separation of the weld.

8. Concluding remarks

This study investigates the conduction welded skin-stringer interface of the thermoplastic composite fuselage demonstrator of the STUNNING project, for which three-stringer panels are successfully designed, analysed and tested.

At first, a fuselage section is analysed to determine the buckling and failure behaviour, which is used as reference behaviour for the design of the panels. The critical failure mode is skin-stringer separation in post-buckling, with separation starting from underneath the stringer and growing in an outwards direction. The preliminary analysis of the three-stringer panel shows similar structural behaviour, with the main difference being the higher number of failure locations, which can be caused by the difference in boundary conditions.

Then, two three-stringer panels are manufactured and tested. The two panels show a similar pre-buckling stiffness, buckling load and initial buckling shape. It is however observed that only one panel changes buckling shape in post-buckling from a three half-wave shape to a four half-wave shape. The welded joint is able to withstand the deformation of post-buckling till a considerable high load, with the ratio between buckling load and final failure load being 1.94 and 1.87

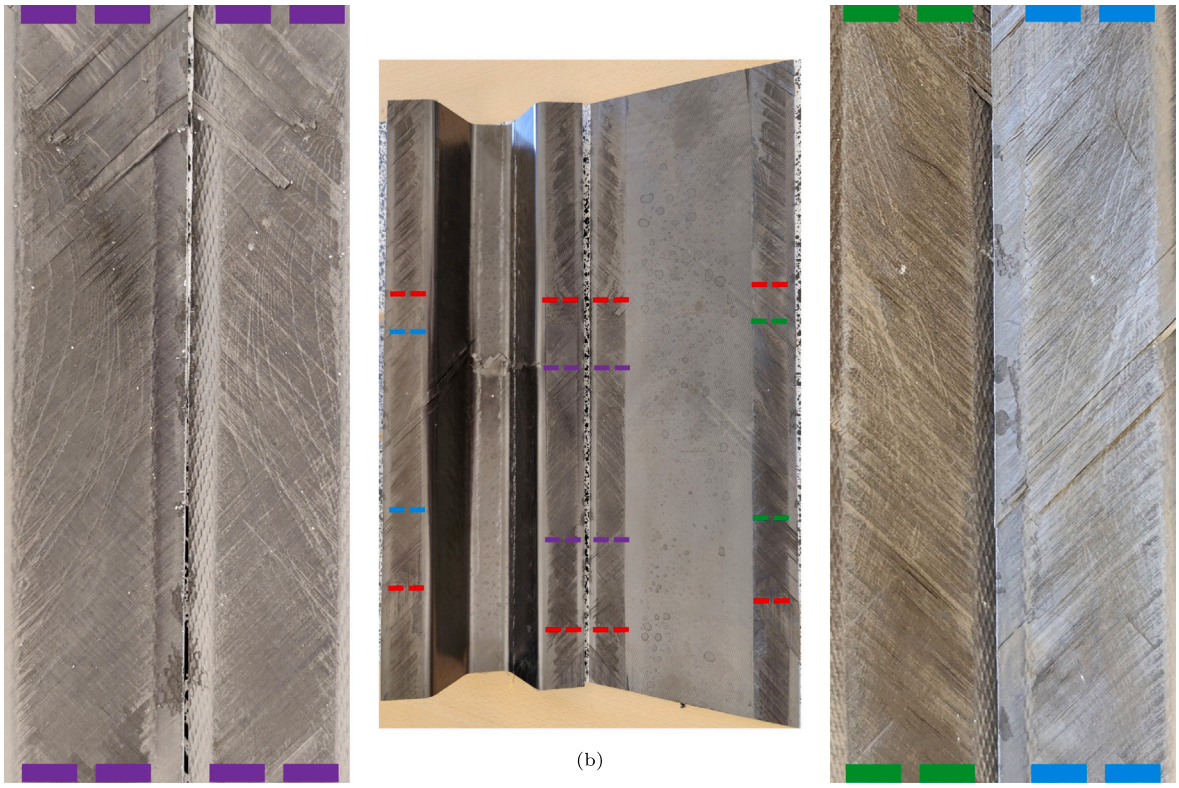

Fig. 27. Weld fracture surfaces of panel 1 middle stringer: (a) close-up of the left weld, with the area between purple dashes; (b) welds middle stringer, with the area in between red dashes corresponding to the separated area in the test; (c) close-up of the right weld, with the area between blue and green dashes.

for panels 1 and 2, respectively. The panels fail in post-buckling due to skin-stringer separation, with no material failure before the start of separation.

Skin-stringer separation appears to start from underneath the stringer, with separation growth in both the longitudinal direction and outward direction. The number of half-waves underneath the stringer increases before final failure, which indicates that the buckling shape underneath the stringer is an important factor.

Further numerical analyses of the two panels are conducted, which include imperfections from DIC and laminate thickness imperfections based on measurements of the manufactured panels. The overall structural behaviour of the two panels is accurately predicted, with a slight difference in the buckling shape evolution of panel 1 between the test and prediction. The skin-stringer separation behaviour is also predicted well.

The results obtained in this research do show that the methodology is a reliable tool for the analysis of welded panels in post-buckling. The post-buckling performance of the welded panels, and the predictable structural behaviour, show great promise for the use of thermoplastic composites for primary structures.

CRediT authorship contribution statement

Kevin van Dooren: Conceptualization, Methodology, Software, Validation, Investigation, Visualization, Writing – original draft, Editing. **Chiara Bisagni:** Conceptualization, Methodology, Investigation, Resources, Writing – review & editing, Supervision.

Declaration of competing interest

The authors declare that they have no known competing financial interests or personal relationships that could have appeared to influence the work reported in this paper.

Data availability

Data will be made available on request.

Acknowledgements

This project has received funding from the Clean Sky 2 Joint Undertaking (JU) under grant agreement No 945583. The JU receives support from the European Union's Horizon 2020 research and innovation programme and the Clean Sky 2 JU members other than the Union. The authors thank GKN Fokker and NLR — Netherlands Aerospace Centre, for the manufacturing and welding of the test panels.

Disclaimer

The results, opinions, conclusions, etc. presented in this work are those of the authors only and do not necessarily represent the position of the JU; the JU is not responsible for any use made of the information contained herein.

References

[1] Tijs BHAH, van Dooren KS, Bisagni C. Development of a numerical framework for virtual testing to support design of a next generation thermoplastic multifunctional fuselage. In: II European conference on multifunctional structures. 2020, http://dx.doi.org/10.23967/emus.2020.005.

[2] Omairey SL, Sampethai S, Hans L, Worrall C, Lewis S, Negro D, Sattar T, Ferrera E, Blanco E, Wighton J, Muijs L, Veldman SL, Doldersum M, Tonnaer R, Jayasree N, Kazilas M. Development of innovative automated solutions for the assembly of multifunctional thermoplastic composite fuselage. Int J Adv Manuf Technol 2021;117(5):1721–38.

[3] Tijs BHAH, Doldersum MHJ, Turon A, Waleson JEA, Bisagni C. Experimental and numerical evaluation of conduction welded thermoplastic composite joints. Compos Struct 2022;281:114964. http://dx.doi.org/10.1016/j.compstruct.2021.114964.

[4] Offringa A, van Ingen JW, Buitenhuis A. Butt-joined, thermoplastic stiffened-skin concept development. SAMPE J 2012;48(2):7–15.
[5] van Ingen JW. Thermoplastic orthogrid fuselage shell. SAMPE J 2016;52(5):7–15.
[6] Tijs BHAH, Abdel-Monsef S, Renart J, Turon A, Bisagni C. Characterization and analysis of the interlaminar behavior of thermoplastic composites considering fiber bridging and R-curve effects. Composites A 2022;162:107101. http://dx.doi.org/10.1016/j.compositesa.2022.107101.
[7] Li N, Chen P. Prediction of compression-after-edge-impact (CAEI) behaviour in composite panel stiffened with I-shaped stiffeners. Composites B 2017;110:402–19. http://dx.doi.org/10.1016/j.compositesb.2016.11.043.
[8] Meeks C, Greenhalgh E, Falzon BG. Stiffener debonding mechanisms in post-buckled CFRP aerospace panels. Composites A 2005;36:934–46. http://dx.doi.org/10.1016/j.compositesa.2004.12.003.
[9] Vescovini R, Dávila CG, Bisagni C. Failure analysis of composite multi-stringer panels using simplified models. Composites B 2013;45:939–51. http://dx.doi.org/10.1016/j.compositesb.2012.07.030.
[10] Bertolini J, Castanié B, Barrau JJ, Navarro JP. Multi-level experimental and numerical analysis of composite stiffener debonding. Part 1: Non-specific specimen level. Compos Struct 2009;90(4):381–91. http://dx.doi.org/10.1016/j.compstruct.2009.04.001.
[11] Bertolini J, Castanié B, Barrau JJ, Navarro JP, Petiot C. Multi-level experimental and numerical analysis of composite stiffener debonding. Part 2: Element and panel level. Compos Struct 2009;90:392–403. http://dx.doi.org/10.1016/j.compstruct.2009.04.002.
[12] van Dooren K, Tijs B, Waleson J, Bisagni C. Skin-stringer separation in post-buckling of butt-joint stiffened thermoplastic composite panels. Compos Struct 2023;304:116294. http://dx.doi.org/10.1016/j.compstruct.2022.116294.
[13] Reeder JR. An evaluation of mixed-mode delamination failure criteria. Tech. rep., 1992.
[14] Flanagan M, Doyle A, Doyle K, Ward M, Bizeul M, Canavan R, Weaver B, Ó Brádaigh CM, Harrison NM, Goggins J. Comparative manufacture and testing of induction welded and adhesively bonded carbon fibre PEEK stiffened panels. J Thermoplast Compos Mater 2018;32(12):1622–49. http://dx.doi.org/10.1177/0892705718792362.
[15] Peeters D, Clancy G, Oliveri V, O'Higgins R, Jones D, Weaver PM. Concurrent design and manufacture of a thermoplastic composite stiffener. Compos Struct 2019;212:271–80. http://dx.doi.org/10.1016/j.compstruct.2019.01.033.
[16] Oliveri V, Zucco G, Peeters D, Clancy G, Telford R, Rouhi M, McHale C, O'Higgins RM, Young TM, Weaver PM. Design, manufacture and test of an in-situ consolidated thermoplastic variable-stiffness wingbox. AIAA J 2019;57(4):1671–83. http://dx.doi.org/10.2514/1.j057758.
[17] Brito CBG, Teuwen J, Dransfeld C, Villegas IF. The effects of misaligned adherends on static ultrasonic welding of thermoplastic composites. Composites A 2022;155:106810. http://dx.doi.org/10.1016/j.compositesa.2022.106810.
[18] Brito CBG, Teuwen J, Dransfeld C, Villegas IF. On improving process efficiency and weld quality in ultrasonic welding of misaligned thermoplastic composite adherends. Compos Struct 2023;304:116342. http://dx.doi.org/10.1016/j.compstruct.2022.116342.
[19] Kolanu NR, Raju G, Ramji M. A unified numerical approach for the simulation of intra and inter laminar damage evolution in stiffened CFRP panels under compression. Compos. B 2020;190(2020). http://dx.doi.org/10.1016/j.compositesb.2020.107931.
[20] Mo Y, Ge D, He B. Experiment and optimization of the hat-stringer-stiffened composite panels under axial compression. Composites B 2016;84:285–93. http://dx.doi.org/10.1016/j.compositesb.2015.08.039.
[21] Orifici AC, de Zarate Alberdi IO, Thomson RS, Bayandor J. Compression and post-buckling damage growth and collapse analysis of flat composite stiffened panels. Compos Sci Technol 2008;68:3150–60. http://dx.doi.org/10.1016/j.compscitech.2008.07.017.
[22] Riccio A, Raimondo A, Di Felice G, Scaramuzzino F. A numerical procedure for the simulation of skin–stringer debonding growth in stiffened composite panels. Aerosp Sci Technol 2014;39:307–14. http://dx.doi.org/10.1016/j.ast.2014.10.003.
[23] Degenhardt R, Kling A, Rohwer K, Orifici AC, Thomson RS. Design and analysis of stiffened composite panels including post-buckling and collapse. Comput Struct 2008;86(9):919–29. http://dx.doi.org/10.1016/j.compstruc.2007.04.022, Composites.
[24] Orifici AC, Thomson RS, Degenhardt R, Kling A, Rohwer K, Bayandor J. Degradation investigation in a postbuckling composite stiffened fuselage panel. Compos Struct 2008;82(2):217–24. http://dx.doi.org/10.1016/j.compstruct.2007.01.012.
[25] Bisagni C, Vescovini R, Dávila CG. Single-stringer compression specimen for the assessment of damage tolerance of postbuckled structures. J Aircr 2011;48(2):495–502. http://dx.doi.org/10.2514/1.C031106.
[26] Raimondo A, Doesburg SA, Bisagni C. Numerical study of quasi-static and fatigue delamination growth in a post-buckled composite stiffened panel. Compos B 2020;182(2020). http://dx.doi.org/10.1016/j.compositesb.2019.107589.
[27] Paz J, Raimondo A, Bisagni C. Experimental study of post-buckled single-stringer composite specimens under fatigue loads with different load levels and load ratios. Composites B 2023;110606. http://dx.doi.org/10.1016/j.compositesb.2023.110606.
[28] Kootte L. A Methodology to Reproduce Postbuckling in Composite Panels to Study Skin Stringer Separation, PhD thesis, Delft University of Technology; 2023.
[29] Wichita State University NCAMP. Medium toughness PAEK thermoplastics Toray (formerly TenCate) cetex TC1225 (LM PAEK) T700GC 12K T1E unidirectional tape 145 gsm 34% RC qualification material property data report. 2020.
[30] Abaqus 2021 documentation. Dassault Systemes Simulia Corp.; 2021.
[31] Krueger R. An approach to assess delamination propagation simulation capabilities in commercial finite element codes. NASA technical memorandum NASA/TM-2008-215123, 2008.
[32] Krueger R. A summary of benchmark examples to assess the performance of quasi-static delamination propagation prediction capabilities in finite element codes. J Compos Mater 2014;49:3297–316. http://dx.doi.org/10.1177/0021998314561812.
[33] Camanho PP, Dávila CG, de Moura MF. Numerical simulation of mixed-mode progressive delamination in composite materials. J Compos Mater 2003;37(16):1415–38. http://dx.doi.org/10.1177/0021998303034505.